



# Assessment of divergent functional properties of seed-like strontium molybdate for the photocatalysis and electrocatalysis of the postharvest scald inhibitor diphenylamine



Raj Karthik<sup>a</sup>, Natarajan Karikalan<sup>a</sup>, Shen-Ming Chen<sup>a,\*</sup>, Jeyaraj Vinoth Kumar<sup>b</sup>, Chelladurai Karupiah<sup>c</sup>, Velluchamy Muthuraj<sup>b</sup>

<sup>a</sup>Electroanalysis and Bioelectrochemistry Lab, Department of Chemical Engineering and Biotechnology, National Taipei University of Technology, No. 1, Section 3, Chung-Hsiao East Road, Taipei 106, Taiwan, Republic of China

<sup>b</sup>Department of Chemistry, VHNSN College, Virudhunagar 626001, Tamil Nadu, India

<sup>c</sup>Battery Research Center of Green Energy, Ming Chi University of Technology, New Taipei City 24301, Taiwan, Republic of China

## ARTICLE INFO

### Article history:

Received 16 April 2017

Revised 31 May 2017

Accepted 1 June 2017

### Keywords:

Carbazole

Radical cations

Interference

Photocatalysis

Electrocatalysis

Strontium molybdate

## ABSTRACT

The bifunctional activity of strontium molybdate (SrMoO<sub>4</sub>) in the photodegradation and electrocatalytic determination of diphenylamine (DPAH) was identified and demonstrated. The photocatalytic and electrocatalytic activity of SrMoO<sub>4</sub> were influenced by its structural properties. Those structural properties are scrutinized by various physical spectroscopic and microscopic tools. In this work, we mainly concentrated on two phenomena of SrMoO<sub>4</sub>, the photon absorption and electrochemical behavior. UV–visible spectroscopy was used to assess the photon absorption characteristics of SrMoO<sub>4</sub>, which mostly generates OH<sup>•</sup> radicals for the degradation of DPAH. The rate of photodegradation was demonstrated in terms of irradiation time, pH, catalyst loading, and initial concentration. On the other hand, voltammetry was used to evaluate the electrochemical behavior of SrMoO<sub>4</sub>. The overall reaction pathways of DPAH showed that the major contribution of the reaction is generation of radical cations (DPAH<sup>•+</sup>). Therefore, we can determine the concentration of DPAH by measuring DPAH<sup>•+</sup>. Differential pulse voltammetry is a suitable analytical tool to measure DPAH<sup>•+</sup>, which determined the DPAH in the linear range 0.1–35 μM and with a lowest detection limit of 30 nM. One of the greatest challenges of this determination is the selectivity, because DPAH<sup>•+</sup> is highly reactive toward similar functionalities such as anions and cations. Therefore, we carefully investigated and discussed the selectivity in the presence of interfering compounds.

© 2017 Elsevier Inc. All rights reserved.

## 1. Introduction

Over the past two decades, the alkaline-earth metal molybdates (AMoO<sub>4</sub>; A = Mg, Ca, Sr, and Ba) have been extensively studied in terms of structure and physicochemical properties. Mostly, the scheelite-type structure (bivalent cations) exhibits excellent strength, high decomposition temperature, and chemical and thermal stability [1]. In particular, calcium molybdate (CaMoO<sub>4</sub>) was focused on due to its admirable photoluminescence properties, and it has been used as an anode material for Li ion batteries, solid-state lasers, solar cells, scintillators in medical devices, and fiber optic communications [2–6]. However, strontium molybdate (SrMoO<sub>4</sub>) has received little attention. Past studies documented its structural evolutions by high-pressure X-ray diffraction and neutron diffraction patterns [7,8]. Also, its crystal growth has been

investigated under various precipitation conditions [9]. In addition, various synthesis methodologies have been developed to control its morphology, such as co-precipitation [10], microwave irradiation [11], hydrothermal methods [12], microwave hydrothermal preparation [13], and solid-state metathetic synthesis [14]. The detailed structural studies are well documented but the applications of SrMoO<sub>4</sub> have not yet been studied. Hence, the present study concentrates on the electrochemical and photochemical applications of SrMoO<sub>4</sub>. The photochemical properties of SrMoO<sub>4</sub> are investigated for the [MoO<sub>4</sub>]<sup>2-</sup> tetrahedral unit, which absorbs light energy in the UV region and possibly contributes to photoluminescence properties [6]. On the other hand, the electrochemical properties of SrMoO<sub>4</sub> are inferred from the charge distribution between Sr<sup>2+</sup> and [MoO<sub>4</sub>]<sup>2-</sup> units. Inspired by these facts, we have applied SrMoO<sub>4</sub> to the electrochemical determination and photocatalytic degradation of diphenylamine (DPAH).

DPAH is a derivative of aniline and is mostly used as a postharvest scald inhibitor for apples and pears because of its excellent

\* Corresponding author.

E-mail address: [smchen78@ms15.hinet.net](mailto:smchen78@ms15.hinet.net) (S.-M. Chen).

antioxidant properties, which protect the skins of apples and pears by preventing the oxidation of  $\alpha$ -farnesene in cold storage [15]. Industrially, there are several processes using DPAH, despite its low solubility, because of which it remains on the skins of apples and pears, and thus persists in fruit juices. Further, wastewater from storage factories is highly contaminated with DPAH and its derivatives. DPAH damages red blood cells, which causes erythropoiesis and hemosiderosis [16]. Therefore, DPAH is listed as a priority pollutants by the European Union (EU); EU directive 91/414/EEC establishes a maximum allowed concentration of DPAH of 5–10 mg kg<sup>-1</sup> [17]. Hence, the determination of DPAH is of considerable importance.

Hitherto, limited analytical procedures have been developed to determine DPAH, such as gas chromatography, high performance liquid chromatography, mass spectrometry, and spectrophotometry [18–21]. These techniques are quite costly and need instruments operated by highly skilled technicians. Electrochemistry offers an alternative method to determine the DPAH. To the best of our knowledge, there is only one report available for the electrochemical determination of DPAH by molecularly imprinted polymers [22]. Herein, we have developed an effective and efficient sensing platform to determine DPAH using SrMoO<sub>4</sub> catalyst.

The photodegradation of DPAH has been investigated in various pH solutions and for different irradiation times. Here also, only one report is available for the mechanistic investigation of DPAH degradation by a mixture of acetonitrile and DPAH [23]. As described in the literature, most of the reaction proceeds through OH radicals by which the oxidation of DPAH yields radicals on an aromatic ring. These radicals are further delocalized to produce aniline-type radicals. This reaction is initiated through radical formation on the aromatic ring or the aromatic amine group. Afterward, these radicals are rearranged to form a covalent bond between two aromatic rings or to initiate degradation of DPAH to other byproducts. The authors monitored direct photolysis by a liquid chromatographic–mass spectrometric technique and analyzed the byproducts. Finally, they concluded that the major degradation product is carbazole (CBZ). Following their work, we investigated the photodegradation of DPAH by time-dependent UV–visible spectra and proposed a photocatalytic mechanism for SrMoO<sub>4</sub> by the scavenger profile. This heterogeneous photocatalyst generates the OH<sup>•</sup> radicals that are the primary active species targeting the DPAH.

## 2. Experimental

### 2.1. Materials

Strontium chloride (SrCl<sub>2</sub>), sodium molybdate (Na<sub>2</sub>MoO<sub>4</sub>), diphenylamine (DPAH, C<sub>12</sub>H<sub>11</sub>N), magnesium chloride (MgCl<sub>2</sub>), sodium chloride (NaCl), calcium chloride (CaCl<sub>2</sub>), urea (CH<sub>4</sub>N<sub>2</sub>O), diuron (C<sub>9</sub>H<sub>10</sub>C<sub>12</sub>N<sub>2</sub>O), carbofuran (C<sub>12</sub>H<sub>15</sub>NO<sub>3</sub>), chlorpyrifos (C<sub>9</sub>H<sub>11</sub>C<sub>13</sub>NO<sub>3</sub>PS), and all other chemicals were purchased from Sigma-Aldrich and Alfa Aesar companies and used as received without further purification. A phosphate buffer (PB) electrolyte solution was prepared by using a mixture of monosodium phosphate (NaH<sub>2</sub>PO<sub>4</sub>) and disodium phosphate (Na<sub>2</sub>HPO<sub>4</sub>). All required solutions were prepared using double-distilled (DD) water.

### 2.2. Apparatus and electrochemical measurements

The structural characterization of seed-like SrMoO<sub>4</sub> was carried out by powder X-ray diffraction (XRD) on a Rigaku MiniFlex II instrument. Fourier transform infrared spectroscopy (FT-IR) was performed using an FT/IR-6600 spectrophotometer. The Raman spectrum was obtained using a Raman spectrometer (Dong Woo 500i, Korea) equipped with a charge-coupled detector. The X-ray

photoelectron spectra (XPS) of SrMoO<sub>4</sub> were obtained using a ULVAC-PHI 5000 Versa Prob X-ray photoelectron spectrometer. The surface morphology was probed by transmission electron microscopy (TEM- TECNAI G2). Scanning electron microscopy (SEM) and energy dispersive X-ray spectral studies were carried out with a Hitachi S-3000 H scanning electron microscope (SEM Tech Solutions, USA) and HORIBA EMAX X-ACT, respectively. The electrocatalytic behavior and the detection of DPAH were performed by cyclic voltammetry (CV) and differential pulse voltammetry (DPV) using CHI 405a and CHI 900 (CH Instruments, USA). A conventional three-electrode system was used for electrocatalytic studies, where the modified GCE is the working electrode (0.07 cm<sup>2</sup>), platinum wire is the auxiliary electrode, and Ag/AgCl is used as a reference electrode.

### 2.3. Preparation of seed-like SrMoO<sub>4</sub>

The seed-like SrMoO<sub>4</sub> was prepared by the simple precipitation method. In a typical synthesis, 40 mL of 0.2 M Na<sub>2</sub>MoO<sub>4</sub> was taken and stirred at 1000 rpm and 40 mL of 0.1 M SrCl<sub>2</sub> was added to the stirred solution of Na<sub>2</sub>MoO<sub>4</sub>. This mixture was then stirred for 1 h. The clear solution of Na<sub>2</sub>MoO<sub>4</sub> was completely turned into a white precipitate while SrCl<sub>2</sub> solution was added. The precipitate was washed with copious amounts of water and absolute ethanol and dried overnight at 80 °C. Finally, the dried SrMoO<sub>4</sub> was annealed at 500 °C for 2 h.

### 2.4. Fabrication of modified electrodes

Before modification, the GCE was polished with 0.05 μm alumina slurry and washed with several amounts of DD water to remove the alumina particles on the GCE surface. The as-prepared seed-like SrMoO<sub>4</sub> was redispersed in DD water and sonicated for 20 min. After that, about 8 μL of seed-like SrMoO<sub>4</sub> suspension was drop coated on the surface of GCE (GCE working area = 0.07 cm<sup>2</sup>). The drop-coated electrodes were allowed to dry at room temperature and then gently rinsed with water to remove the loosely bound particles. These modified electrodes were further used for the electrochemical characterizations.

### 2.5. Photocatalytic activity of SrMoO<sub>4</sub>

The photocatalytic activity of the as-synthesized SrMoO<sub>4</sub> for the degradation of DPAH solution under visible light irradiation was evaluated. For these photocatalysis measurements, our previously reported procedure was followed with a slight modification [24,25]. In a typical procedure, 50 mg of the catalysts was dispersed in 100 mL of DPAH solution (20 mg/L) and stirred for 2 h under dark conditions to reach adsorption–desorption equilibrium between the DPAH solution and the catalyst. After that, the suspension was irradiated with light: a 500 W tungsten incandescent lamp ( $\lambda > 400$  nm) was used as the light source. At 5 min time intervals, 4 mL of the suspensions was collected and the concentration change of DPAH was monitored by a UV–vis spectrophotometer. In a recycle test, the seed-like SrMoO<sub>4</sub> photocatalyst was separated from the reaction mixture by centrifugation after the photodegradation experiments and washed with water, and then dried and used again.

## 3. Results and discussion

### 3.1. Characterizations

The structure and crystal lattice parameters of the as-prepared SrMoO<sub>4</sub> were examined by XRD pattern analysis and are shown in Fig. 1A. The obtained discrete peaks at 18.0°, 27.6°, 29.7°, 33.2°,

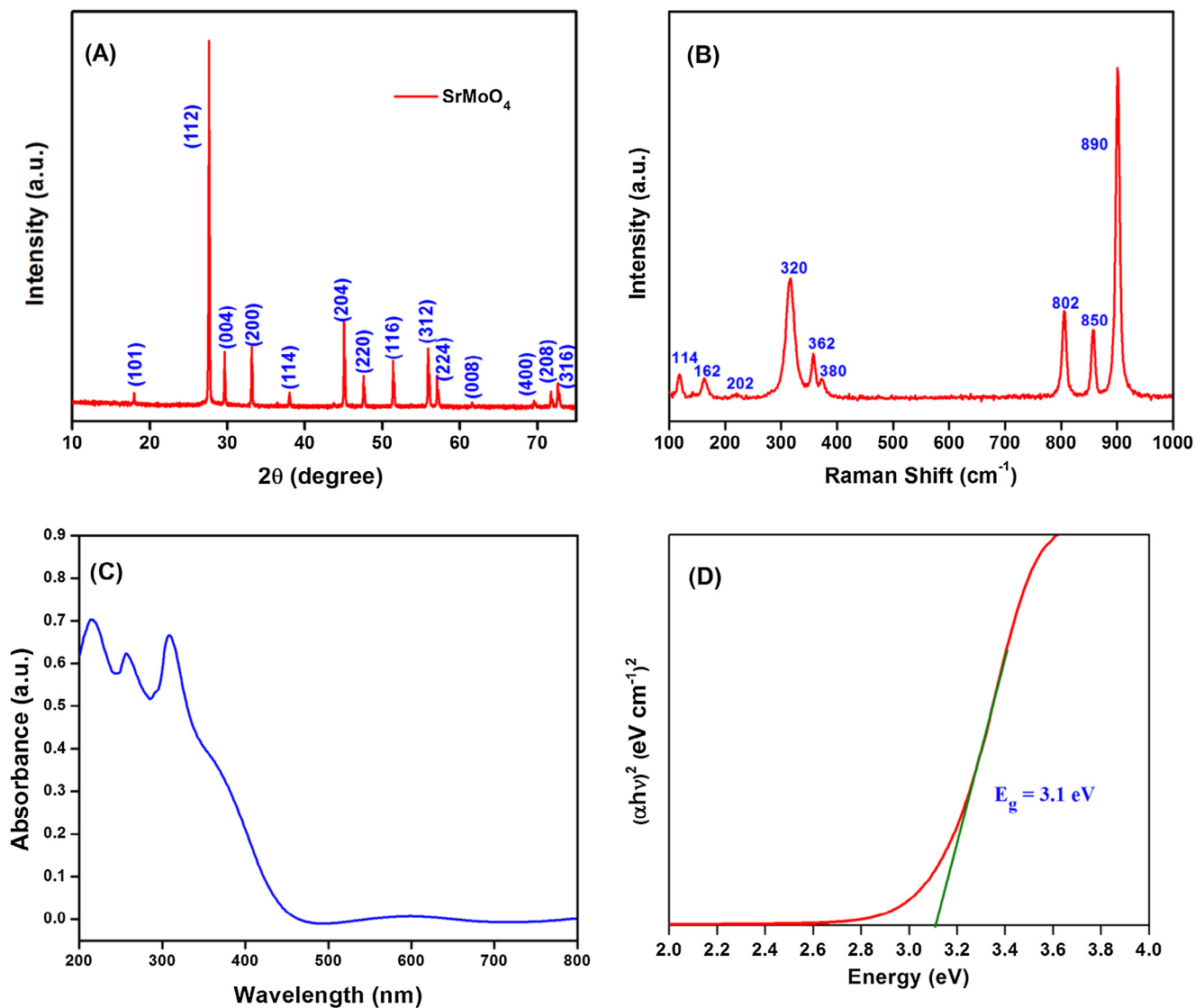


Fig. 1. The X-ray diffraction patterns (A), Raman spectrum (B), UV-DRS (C), and Tauc plot (D) of SrMoO<sub>4</sub>.

38.1°, 45.1°, 47.6°, 51.5°, 55.9°, 57.1°, 61.7°, 69.7°, 71.8°, and 72.7° correspond to the (1 0 1), (1 1 2), (0 0 4), (2 0 0), (1 1 4), (2 0 4), (2 2 0), (1 1 6), (3 1 2), (2 2 4), (0 0 8), (4 0 0), (2 0 8), and (3 1 6) planes, respectively. All the observed peaks are closely matched with the reference peaks of JCPDS file No: 08-0482, which suggests that SrMoO<sub>4</sub> crystallizes in tetragonal phase with  $a = b = 5.406$  Å and  $c = 12.01$  Å. No additional peaks were observed for the impurities, which means there is no individual SrO or MoO<sub>3</sub> present in SrMoO<sub>4</sub> [26]. The complete crystal structure of SrMoO<sub>4</sub> consists of Sr, Mo, and O, where the Mo ions coordinate with the O ions tetrahedrally and the Sr ions coordinate with the O ions in polyhedral arrangements [8,26,27]. The structure was split into two groups, internal and external; the internal group is [MoO<sub>4</sub>]<sup>2-</sup> and the external group is Sr<sup>2+</sup> in rigid [MoO<sub>4</sub>]<sup>2-</sup> units [27]. The Raman spectra clearly distinguish these two groups by active vibration modes. Fig. 1B shows the Raman spectrum of SrMoO<sub>4</sub> excited by a 531.8 nm laser. The observed vibrations are associated with the internal (related to the [MoO<sub>4</sub>]<sup>2-</sup> stationary mass center) and external groups (related to the motion of Sr<sup>2+</sup> in the rigid [MoO<sub>4</sub>]<sup>2-</sup> groups). When the free space is considered, [MoO<sub>4</sub>]<sup>2-</sup> is present in tetrahedral ( $T_d$ ) symmetry and composed of four internal modes, one free rotation mode, and one translation mode. Due to the crys-

tal field effect, these all degenerative vibrations are split into 26 different types of vibrations ( $\Gamma = 3A_g + 5A_u + 5B_g + 3B_u + 5E_g + E_u$ ) [28].

In all, 13 vibrations are Raman active. The internal modes  $\nu_1(A_g)$ ,  $\nu_2(E_g)$ ,  $\nu_3(E_g)$ , and  $\nu_4(B_g)$  are observed at 890, 850, 802, 380, 362, and 320 cm<sup>-1</sup>. The free rotation mode and the external modes were detected at 200 and at 162 and 114 cm<sup>-1</sup>, respectively. The peak at 802 cm<sup>-1</sup> indicates doubly bonded oxygen, which means the asymmetric stretching vibration of O—Mo—O in the [MoO<sub>4</sub>]<sup>2-</sup> tetrahedron. There is no peak for the singly bonded oxygen Mo—O stretching vibration. However, a peak appears at 380 cm<sup>-1</sup> for the bending vibration of Mo—O of the  $A_u$  mode. This Raman result shows that the motion of Sr<sup>2+</sup> is restricted in the rigid [MoO<sub>4</sub>]<sup>2-</sup> groups [28]. This phenomenon greatly reduces the band gap of MoO<sub>3</sub> when Sr<sup>2+</sup> is introduced into its lattice. The band gap of SrMoO<sub>4</sub> is calculated from the UV-visible diffuse reflectance spectra (UV-DRS) spectra using the Tauc plot. Fig. 1C and D show the UV-DRS spectra and Tauc plot for SrMoO<sub>4</sub>, which shows the calculated band gap of SrMoO<sub>4</sub> to be 3.1 eV.

Further, the elements and their oxidation states in SrMoO<sub>4</sub> were examined by X-ray photoelectron spectroscopy (XPS). Fig. 2A shows the XPS survey spectra of SrMoO<sub>4</sub>, which reveal the respec-

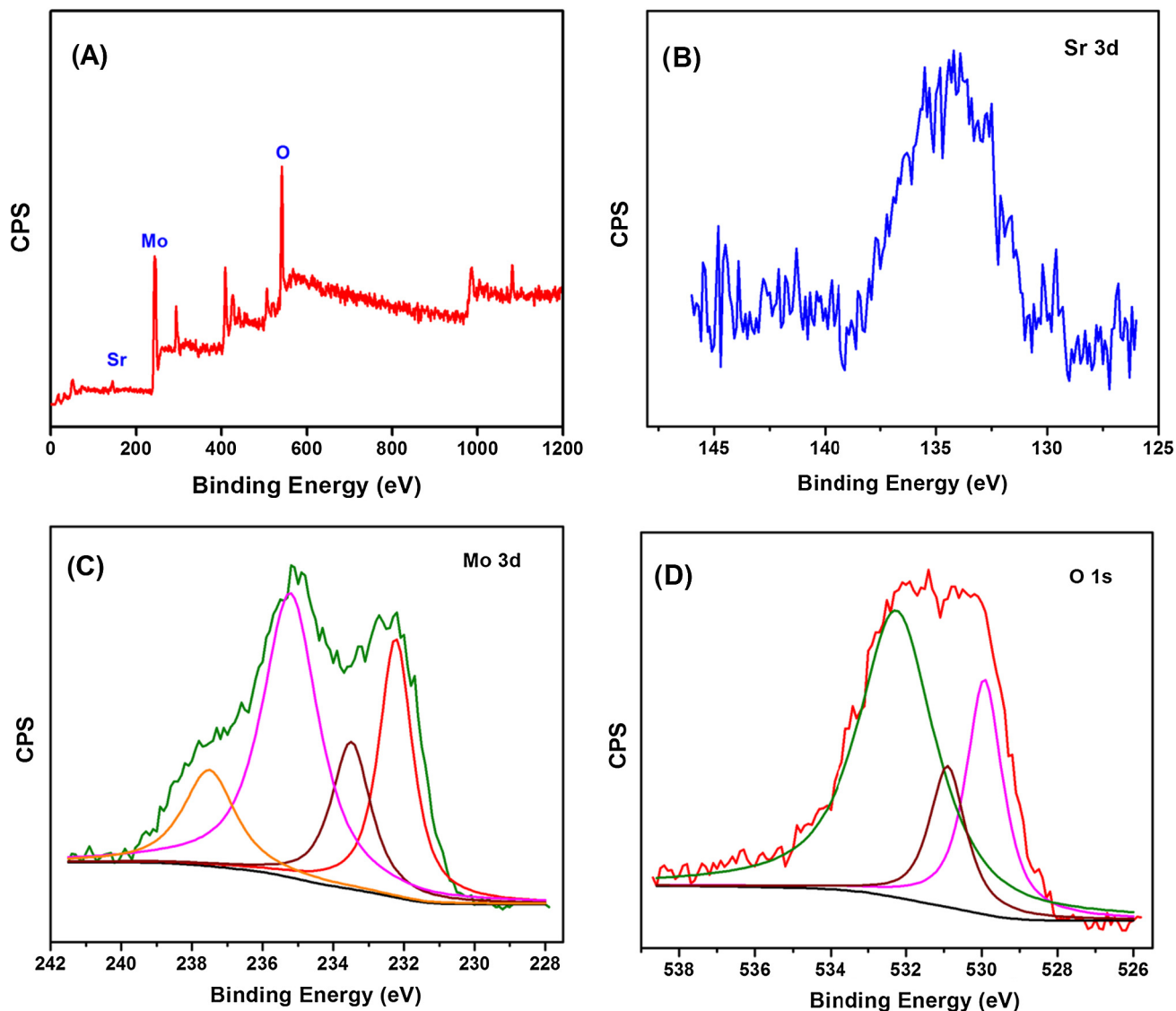
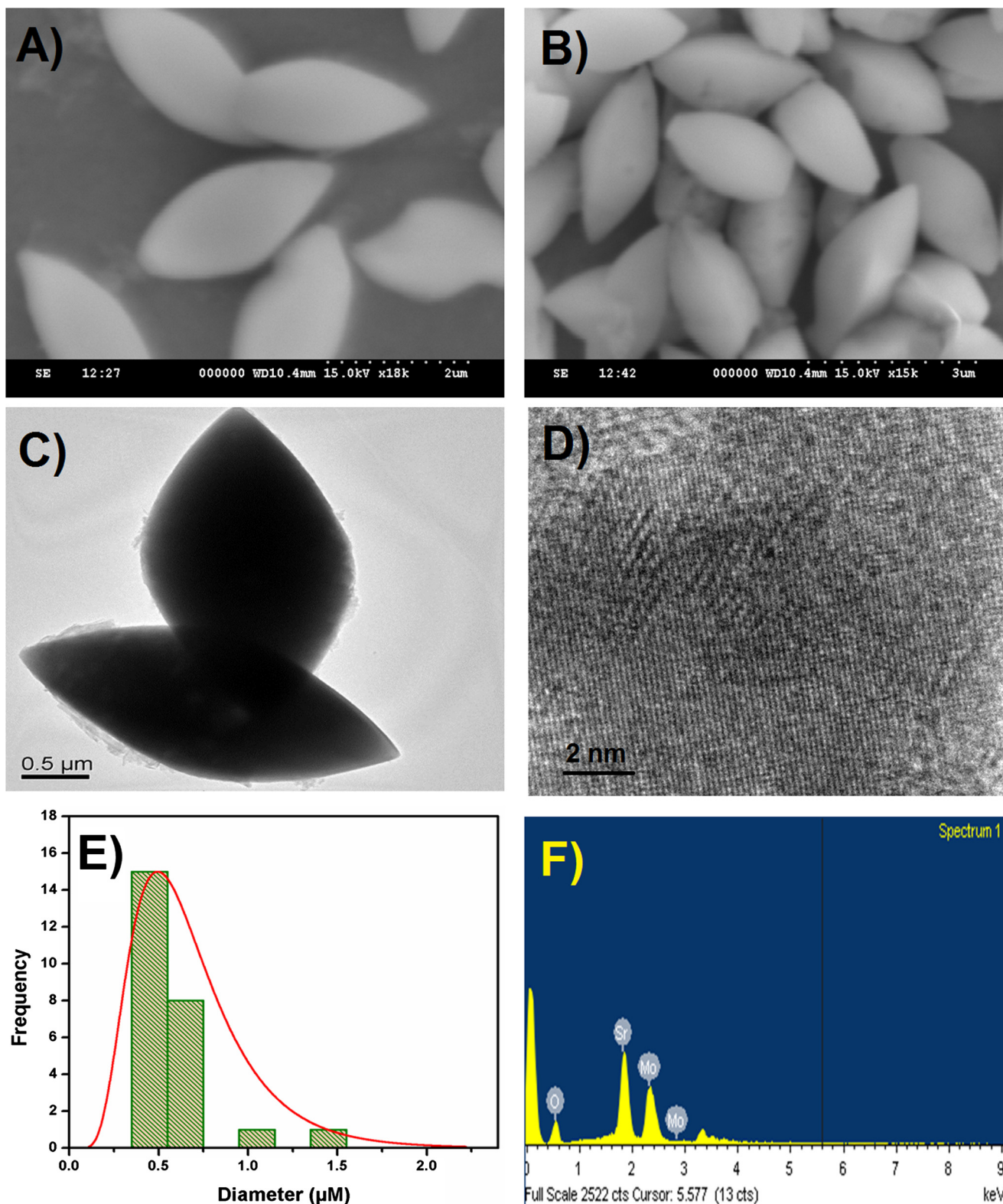


Fig. 2. The XPS survey spectrum (A) and the high-resolution XPS spectra of Sr3d (B), Mo3d (C) and O1s (D) of SrMoO<sub>4</sub>.

tive signals for Mo, Sr, and O, which agreed closely with EDAX analysis (Fig. 3F). Fig. 2C shows the high-resolution XPS spectra of Mo3d, which are further deconvoluted into four peaks for the +5 and +6 oxidation states. The peaks at 232.2 and 235.3 eV correspond to the Mo<sup>6+</sup>3d<sub>5/2</sub> and Mo<sup>6+</sup>3d<sub>3/2</sub>, suggesting stoichiometric MoO<sub>3</sub> [29]. However, the peaks at 230.1 and 233.2 eV are attributed to Mo<sup>5+</sup>3d<sub>5/2</sub> and Mo<sup>5+</sup>3d<sub>3/2</sub>, suggesting the presence of Mo<sub>4</sub>O<sub>11</sub> as a dominant phase. In this case, the oxidation state of Mo shuttles between +6 and +5. Here, the lower oxidation state of Mo is experienced from the dangling bonding site of Sr<sup>2+</sup>. The SrO<sub>8</sub> polyhedra's O<sup>2-</sup> ions are trigonally bonded with rigid tetrahedral [MoO<sub>4</sub>]<sup>-</sup> molecular units. This is further inferred from the high-resolution Sr3d spectra (Fig. 2B). The centralized peak at 132.5 eV contains 3d<sub>5/2</sub> and 3d<sub>3/2</sub>, which suggest a single Sr–O bond. Furthermore, the high-resolution O1s spectra have been taken into account (Fig. 2D).

The O1s spectra were deconvoluted into three peaks, which consist of three different bonding environments between Sr and Mo. The peak profile can be fitted as a low-binding-energy component (LBEC) and a high-binding-energy component (HBEC) [30].

The HBEC contribution suggests that the loosely bound oxygen can be removed from the SrMoO<sub>4</sub> during annealing. This will create an oxygen deficiency throughout the molecule that leads to the lower oxidation state of Mo (Mo<sup>5+</sup>). These oxygen vacancies can create free carriers such as electrons, which may be the reason for the semiconducting behavior of SrMoO<sub>4</sub> [31,32]. Finally, the surface features of the as-prepared SrMoO<sub>4</sub> were probed by SEM and TEM. Fig. 3A and B show the low- and high-magnification SEM images of SrMoO<sub>4</sub>, which portray the distinct seed-like morphology at the micrometer scale. This microsize feature is experienced from the high crystallinity of SrMoO<sub>4</sub> with bulk cations (Sr and Mo). The highly crystalline nature of SrMoO<sub>4</sub> results in excellent photocatalytic activity. Moreover, the TEM images (Fig. 3C) show that the as-prepared SrMoO<sub>4</sub> has semitransparency to electrons. This semitransparent behavior of SrMoO<sub>4</sub> was achieved through the annealing process. Fig. 3D shows a high-magnification TEM image of SrMoO<sub>4</sub>, which clearly shows the lattice patterns for the crystalline planes; the observed *d*-spacings between the planes are perfectly matched with the XRD results. From the TEM images, the length and width of the SrMoO<sub>4</sub> parti-



**Fig. 3.** The high-magnification (A) and low-magnification (B) SEM images of seed-like SrMoO<sub>4</sub> and the HRTEM images (C and D) of SrMoO<sub>4</sub>. The histogram of the particle size distribution (E) and the EDAX spectrum of as-prepared seed-like SrMoO<sub>4</sub> (F).

cles were calculated as 1.5 and 0.5 μm, respectively. Moreover, a statistical analysis was performed for the particle distribution and the data are given in Fig. 3E. The calculated particle sizes are based on the diameter of the seeds, where the maximum diameters of the particles are distributed between 0.35 and 0.75 μm.

### 3.2. Photocatalysis

The photocatalytic degradation of DPAH on SrMoO<sub>4</sub> is investigated for various DPAH solutions under visible light irradiation. The sequential changes in the DPAH concentrations are scrutinized

by observing the absorption variations in UV–vis spectra at 280 nm [23]. Prior to the study of the photocatalytic activity, blank (without catalyst) and dark (in the absence of light) experiments are evaluated. Fig. 4A shows the photodegradation of DPAH without catalyst and the absence of light experiment, which shows that the photocatalytic activity is negligible. Therefore, photolysis of DPAH in the dark or without catalyst is not beneficial; hence further experiments proceed with light and catalyst. Fig. 4B shows the time-dependent UV–vis spectra of DPAH degradation on SrMoO<sub>4</sub> for time intervals of 0–45 min. The results show that the absorption was greatly reduced at 45 min, which means that 99% of the DPAH degradation was achieved in 45 min. In contrast, commercially available TiO<sub>2</sub> and MoO<sub>3</sub> exhibited only 45% and 60% of degradation, respectively. This study concluded that the Sr doping in MoO<sub>3</sub> lattice probably results in enhanced photocatalytic activity. To ensure the efficiency of SrMoO<sub>4</sub>, the various parameters, such as catalyst loading, initial concentration, and pH, are evaluated.

The recombination of holes and electrons considerably suppresses the photocatalytic activity of SrMoO<sub>4</sub>; i.e., the effect of catalyst loading can play a significant role in the control of recombination properties of SrMoO<sub>4</sub> [24]. Therefore, the photocatalytic activity of SrMoO<sub>4</sub> for DPAH degradation was evaluated with

different catalyst loadings ranging from 0.25 to 1 mg/mL, while the concentration of DPAH and light sources remained constant.

Fig. 4C shows the effect of catalyst dosage. The 0.5 mg/mL photocatalyst gave the best activity with 99% degradation efficiency. The remaining dosages are suffering from the recombination of holes and electrons because the effective diffusion of photons is blocked by a high concentration of the photocatalyst [24,25]. Hence, the generations of holes and photons is insufficient when the amount of photocatalyst is increased. Meanwhile, at the lowest dosage, the holes and electrons are completely used by the DPAH; thus a high concentration of DPAH seeks more photoactive species. This also leads to decreasing photocatalytic activity; therefore, the suggested photocatalyst dosage is 0.5 mg/mL for the further experiments. The photodegradation rate directly depends on the initial concentration of the DPAH. Therefore, the photodegradation of DPAH is investigated at concentrations of DPAH ranging from 15 to 30 mg/L with a constant catalyst dosage and light source (Fig. 4D).

It is obvious that the photodegradation rate is decreasing when the concentration of DPAH increases. Most of the organic molecules are absorbing the photons at different energies; the DPAH is absorbing the light at 280 nm. As said in the *Experimental* section, our primary light source exhibits different light energies,

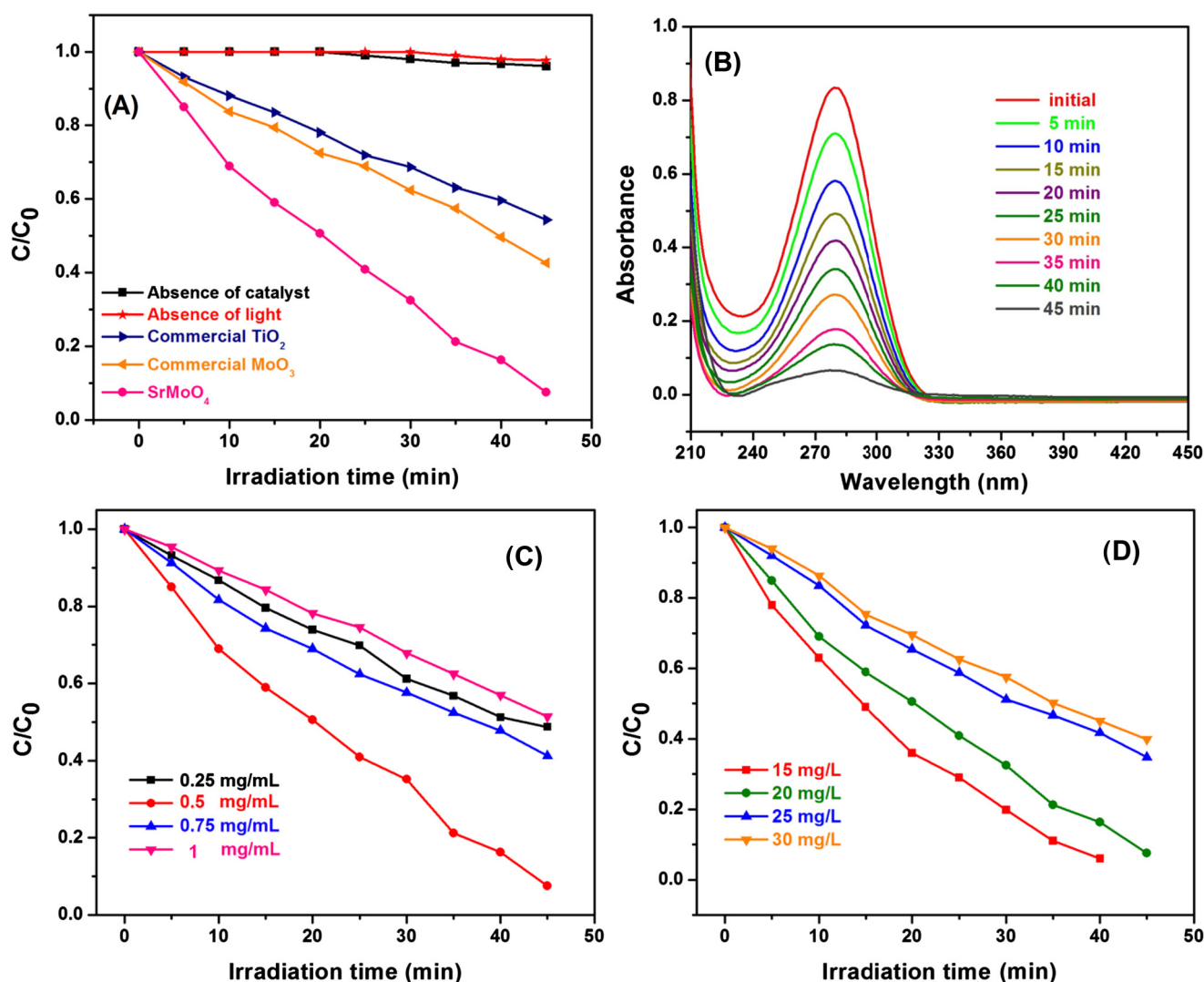
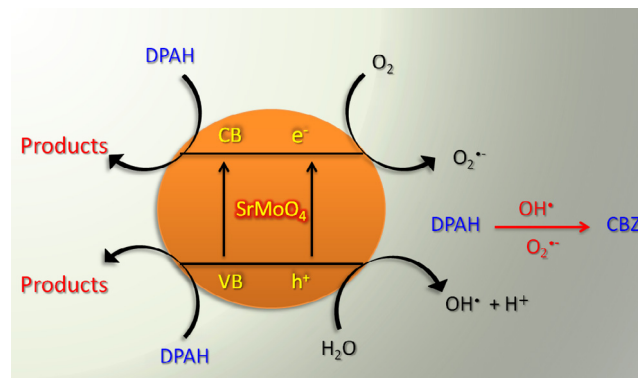


Fig. 4. Comparison of the photodegradation of DPAH on various catalysts with SrMoO<sub>4</sub> in the presence and absence of light and catalyst (A); time-dependent UV–vis absorption spectrum of DPAH photodegradation on SrMoO<sub>4</sub> (B); effect of catalyst dosage of SrMoO<sub>4</sub> on photodegradation (C) and effect of initial concentration of DPAH (D).

which are predominately absorbed by DPAH. Therefore, the consumption of photons is higher for DPAH than for  $\text{SrMoO}_4$ . As a result, the photodegradation rate is decreased when the concentration of DPAH is increased. From this study, 20 mg/L of DPAH is the optimized concentration for degradation efficiency. Furthermore, the solution pH was also investigated because it plays an important role in the generation of active species such as hydroxyl radicals ( $\text{OH}^\cdot$ ) and superoxide radicals ( $\text{O}_2^{\cdot-}$ ). These active species are mainly involved in the degradation of organic molecules. Therefore, it is necessary to investigate the photodegradation rate in different pH solutions of DPAH. Fig. 5A shows the photodegradation of DPAH at different pH from 4 to 12; the pH of the DPAH solution is adjusted by adding HCl (for acidic) and KOH (for basic) [24,25]. The photodegradation rate is increased when the solution pH increases from 4 to 12. This study certifies that the generation of active species is directly proportional to the solution pH. At lower pH, when a high concentration of  $\text{H}^+$  ions turns the  $\text{O}_2^{\cdot-}$  into  $\text{HO}_2^-$ , this  $\text{HO}_2^-$  consumes the  $\text{OH}^\cdot$  and forms  $\text{H}_2\text{O}$  and  $\text{O}_2$ . This process obstructs the reaction between DPAH and the reactive  $\text{OH}^\cdot$ , which results in a decrease in the photodegradation rate. At higher pH, the  $\text{OH}^-$  ions allows the  $\text{H}_2\text{O}$  to react with the CB (conduction band) of  $\text{SrMoO}_4$  and generate more  $\text{OH}^\cdot$  [33]. Sometimes the DPAH reacts directly with the VB (holes,  $\text{h}^+$ ) or CB (electrons,  $\text{e}^-$ ) of  $\text{SrMoO}_4$  and produces byproducts (Scheme 1).

To confirm this active species, we tried to find out how DPAH degrades by investigating the scavenger profile. In this experiment, acrylamide (AA), ammonium oxalate (AO), and *tert*-butyl alcohol (t-BuOH, BA) were used as scavengers for  $\text{O}_2^{\cdot-}$ ,  $\text{h}^+$ , and  $\text{OH}^\cdot$  radicals [33]. For comparison, the photodegradation of DPAH was performed without scavengers and fixed as the standard. Upon addition of scavengers, the photodegradation rate was altered for all the scavengers; however, major changes were observed for the  $\text{OH}^\cdot$  radical scavengers. Fig. 5B shows the rate of photodegradation (%) in the presence and absence of scavengers. BA suppressed 75% of the degradation; this means more than 75% of the reaction was induced by the  $\text{OH}^\cdot$  radicals and the remaining 24% of the reaction was initiated by  $\text{O}_2^{\cdot-}$  and  $\text{h}^+$ . This study identified  $\text{OH}^\cdot$  radicals as the major active species, generated by  $\text{SrMoO}_4$  and contributing strongly to the degradation of DPAH. From the observed results and inspired by previous literature, we have proposed a mechanism of DPAH degradation using  $\text{OH}^\cdot$  radicals.

In Scheme 2, we portray the formation of CBZ by quenching  $\text{OH}^\cdot$  radicals with DPAH. CBZ is the major degradable product, confirmed by the liquid chromatographic-mass spectrometric analysis in the previous literature [23]. Finally, the reusability of  $\text{SrMoO}_4$  was investigated by the stability test. Fig. 5C shows the stability profile of  $\text{SrMoO}_4$  for the photodegradation of DPAH. The six consecutive cycles of the experiment revealed that photocatalytic



**Scheme 1.** Pictorial representation of photocatalytic activity on  $\text{SrMoO}_4$  for the different reaction pathways. Most of the degradation product from the reaction is carbazole (CBZ).

activity on the surface of  $\text{SrMoO}_4$  decreased only 8% from the adsorption of DPAH residues.

### 3.3. Electrocatalysis

The electrochemical behavior of DPAH on bare GCE and  $\text{SrMoO}_4/\text{GCE}$  was examined in a 0.05 M PB solution containing 200  $\mu\text{M}$  DPAH at a scan rate of 50 mV/s. Fig. 6A shows typical cyclic voltammograms of DPAH oxidation for the bare GCE and  $\text{SrMoO}_4/\text{GCE}$ ; the electrocatalytic performances are higher for  $\text{SrMoO}_4/\text{GCE}$ . For the assessment of electrochemical performance, we calculated the electrochemical active surface area for the bare GCE and  $\text{SrMoO}_4$  using the ferricyanide system. For the evaluation, we used the Randles–Sevcik equation. The calculated active surface areas of bare GCE and  $\text{SrMoO}_4$  are 0.038 and 0.052  $\text{cm}^2$ , respectively [34,35]. This higher electroactive surface area is one of the factors that increase the electrocatalytic performance of  $\text{SrMoO}_4$ . Moreover, some other factors influence the electrocatalytic activity: (i) the adsorption of DPAH on the electrode surface, (ii) the oxidation potentials of the highest occupied molecular orbitals (HOMO) of the electrode surface being higher than the lowest unoccupied molecular orbital (LUMO) of DPAH, and (iii) the electrode–electrolyte interfacial properties. These factors promote higher electrochemical performance by the  $\text{SrMoO}_4$ . In Fig. 6A, a strong oxidation peak (peak 1) appears at 0.62 V, corresponding to the one-electron transfer process [22]. This oxidation generates the unstable radical cation  $\text{DPAH}^{\cdot+}$ , which further oxidizes at higher potential; thus, the second peak (peak 2) appears at 0.8 V [36,37]. Upon the reverse scan, no cathodic peaks appeared for the corresponding anodic peaks 1 and 2. This phenomenon showed that the radical cations,

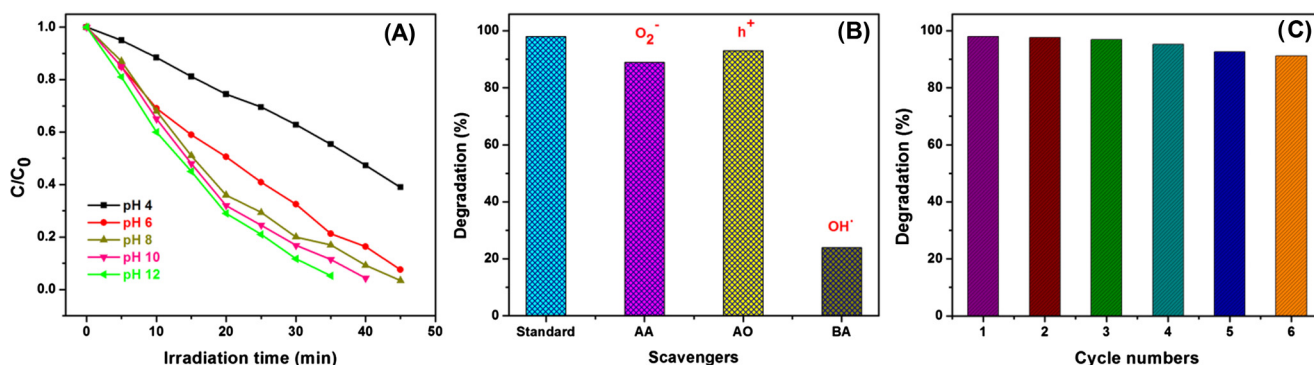
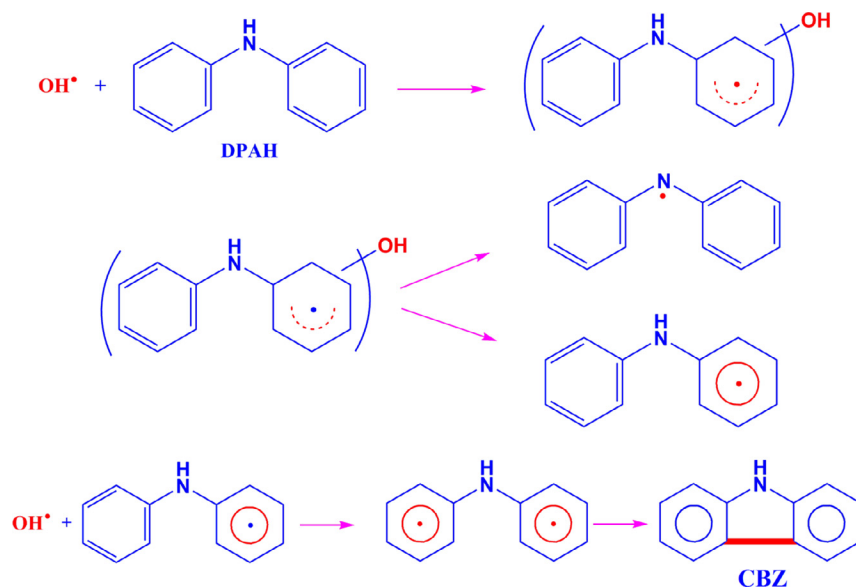


**Fig. 5.** Effect of pH on the photodegradation of DPAH (A), scavenger profile for assessing the primary active species for the photodegradation of DPAH (B), and reusability test for seed-like  $\text{SrMoO}_4$  (C).



**Scheme 2.** A plausible mechanism of the photodegradation of DPAH by the OH· radicals, which produced the aryl radical and led to the formation of carbazole (CBZ).

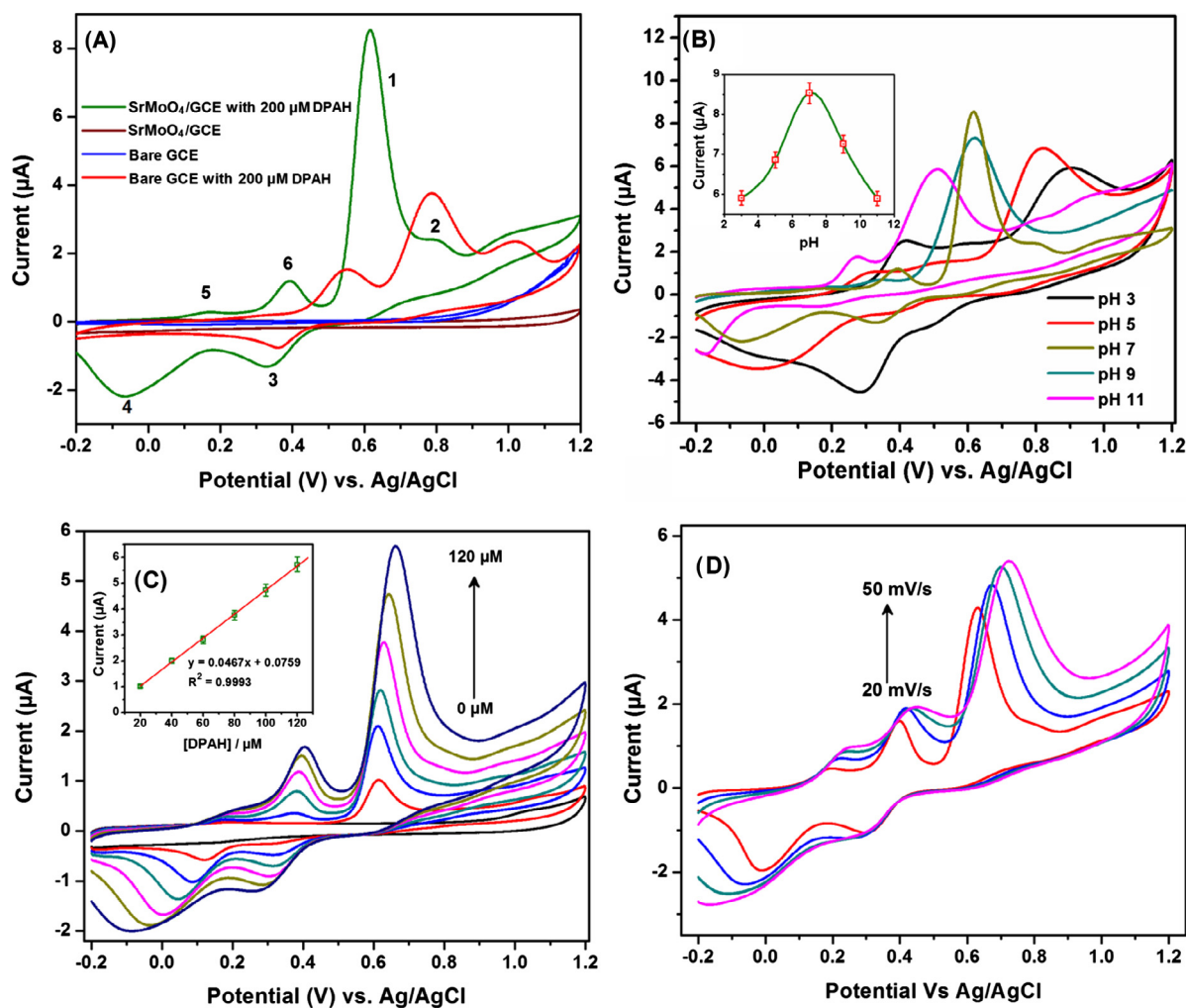
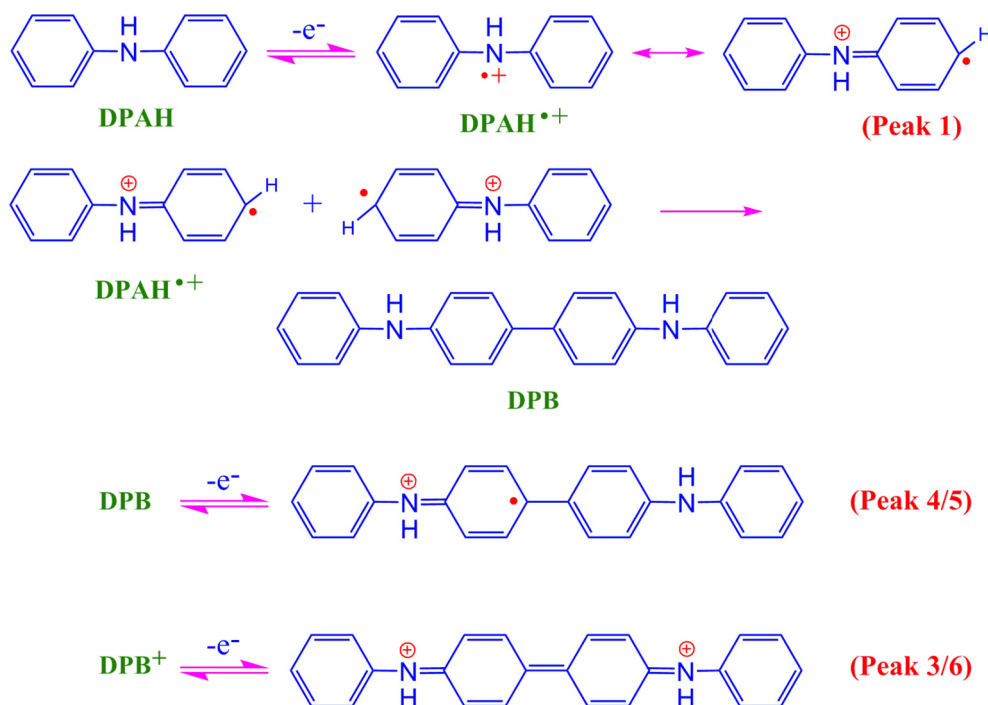


**Fig. 6.** The CVs of bare GCE and SrMoO<sub>4</sub>/GCE in the presence and absence of 200 μM DPAH (A) at a 50 mV/s sweeping rate. Effect of pH on the oxidation of DPAH from 3 to 11 (B); the inset shows the plot of current vs. pH. The effect of various DPAH concentrations for DPAH oxidation on SrMoO<sub>4</sub> from 0 to 120 μM (C); the inset shows the linear relationship between concentration and current ( $i_p$ ). Effect of scan rates on SrMoO<sub>4</sub> on the oxidation of DPAH from 20 to 50 mV/s (D).



**Scheme 3.** The overall mechanism of the electrochemical oxidation of DPAH on the SrMoO<sub>4</sub>.

i.e., DPAH<sup>•+</sup>, were completely reacted together and formed as the dimer (diphenylbenzidine, DPB) [36,37]. Conversely, two well-defined cathodic peaks 3 and 4 were appeared at 0.35 V and -0.25 V and two anodic peaks 5 and 6 were observed at 0.15 and 0.4 V. These anodic peaks 5 and 6 correspond to cathodic peaks 4 and 3, respectively. These redox couples have peak potential separations  $\Delta E_p$  of 60 and 100 mV for 3/6 and 4/5, respectively [37]. From the observed results, we have proposed a mechanism of DPAH oxidation (Scheme 3). In Scheme 3, we illustrate the dimerization of DPAH followed by the formation of cation radicals (DPAH<sup>•+</sup>). The two monomers of the radical cation react together and form a dimer; subsequently, another monomer cation radical reacts with the parent dimer and forms a polymer. There are ways to pair up the radical cations in different couplings, i.e., C–C, C–N, and N–N, that offer different dimerization products [38,39]. The resulting dimers have different structural and physicochemical characteristics, which can be examined by their redox couples in CV. Yang and Bard demonstrated that the CVs of DPB in acetonitrile, which confirmed that the dimer formation happened through C–C coupling only [37]. Guay and Dao demonstrated the C–C coupling by FTIR spectroscopic data, which further confirms that the dimer only forms through the 4,4'-C-C phenyl-phenyl coupling pathway [40]. The repetitive scans in acetonitrile suggest that only DPB is the final product; however, when adding the extra DPAH, it undergoes the electropolymerization at higher anodic potential [37]. However, in PB solution (pH 7), DPAH initially forms DPB and finally is converted into polydiphenylamine. The electropolymerization can be varied at different pHs; thus, we examined the electrocatalytic properties at different pHs.

Fig. 6B shows the CVs of DPAH oxidation at various pHs ranging from 3 to 11. The main oxidation peak (DPAH to DPAH<sup>•+</sup>) shifted to more negative potential when increasing the pH of the electrolyte. The peak shifting in pH is obvious; however, the electropolymerization occurs more in acidic environments and dimerization is favored in alkaline environments. Interestingly, the peak current of DPAH oxidation at pH 3 and 11, 5 and 9 is almost similar (Fig. 6B inset). However, the activity is different at acidic and alkali-

line pHs; the former produced DPAH polymers and the latter produced DPAH dimers. These results were supported by previous literature [37,40]. Moreover, the concentration of DPAH is influencing the electropolymerization process. Fig. 6C shows the CV of the DPAH oxidation at various concentrations ranging from 0 to 120  $\mu$ M of DPAH in 0.05 M PB solution at a scan rate of 50 mV/s.

Primary oxidation peak 1 is linearly increased when the concentration of DPAH increases; however, the two cathodic peaks were shifted to the negative while adding each concentration of DPAH. This result suggested that when the concentration of DPAH increases the reaction favors polymerization. Furthermore, scan rate studies were recommended to investigate the rate of the reaction. Fig. 6D shows the CVs of DPAH oxidation at different scan rates ranging from 20 to 50 mV/s. The peak current of primary oxidation peak 1 was increasing with increasing scan rate; however, the peak potential was slightly shifted to the positive side. For totally irreversible systems, the equilibrium of the reactant and product is not established rapidly. Hence, the diffusion layer contains the byproducts that are obstructing further oxidation. Moreover, the diffusion layer grows much more than the electrode surface at lower scan rates and vice versa at higher scan rates. This diffusion layer creates some internal resistance that further blocks the movement of DPAH from the bulk solution. Therefore, the rate of the reaction was minimized for the consecutive cycles. This result is also in accordance with concentration and pH; hence, these parameters are effectively participating in the polymerization of DPAH. The overall reaction pathways from Scheme 3 indicated that the major contribution of the reaction is the generation of radical cations (DPAH<sup>•+</sup>). Therefore, we can determine the concentration of DPAH by measuring DPAH<sup>•+</sup>.

The differential pulse voltammogram (DPV) is a suitable analytical tool to measure the DPAH<sup>•+</sup>; thus, the DPV was recorded in a 0.05 M PB solution containing various concentrations of DPAH ranging from 0.1 to 83  $\mu$ M. Fig. 7A shows the DPV of DPAH oxidation; the anodic peak for the generation of radical cations (DPAH<sup>•+</sup>) is linearly increased with increasing concentration. The secondary oxidation peaks 5 and 6 do not significantly contribute to the direct

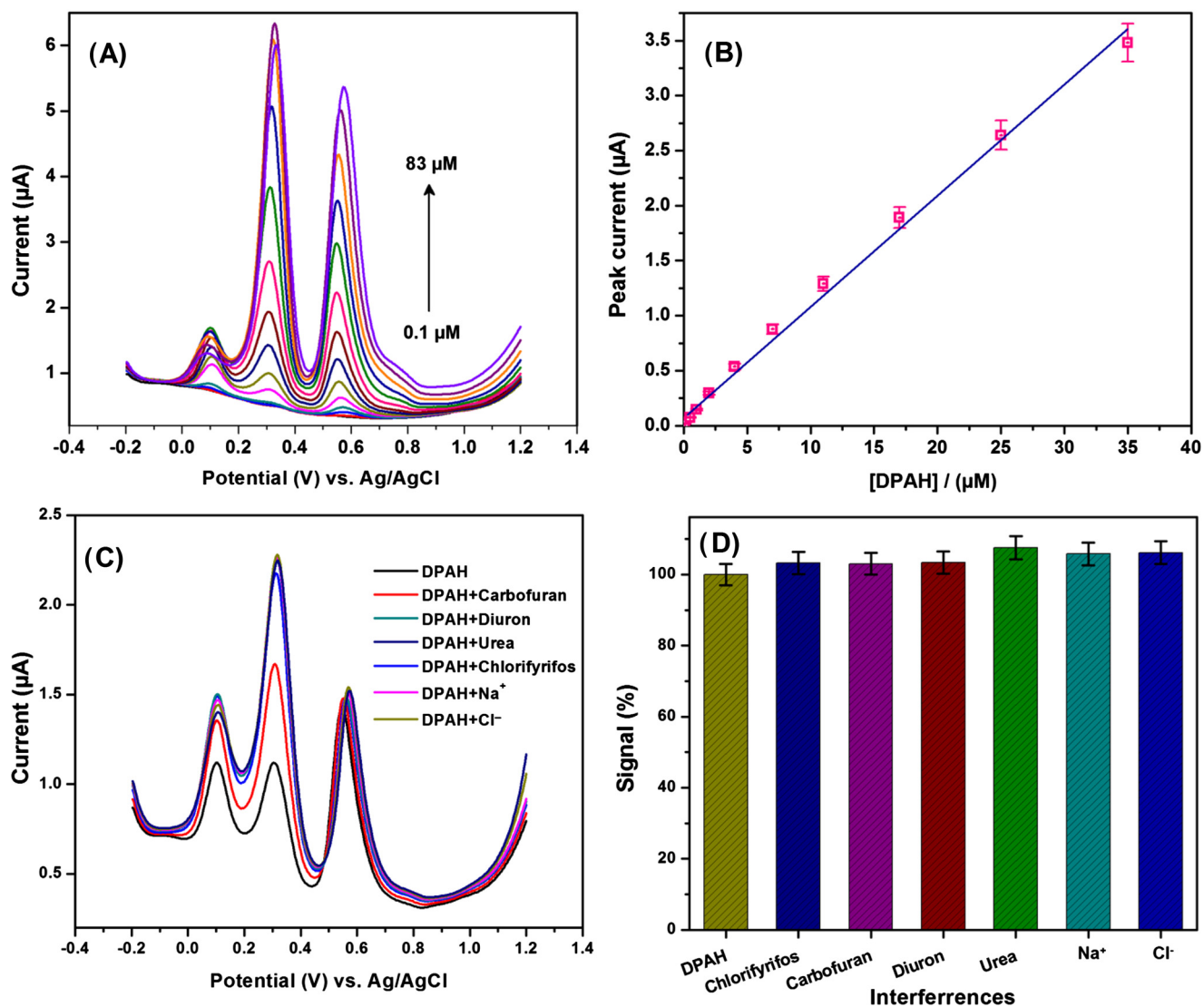


Fig. 7. The DPVs of DPAH oxidation at different concentrations ranging from 0.1 to 83 μM (A), the corresponding calibration plot (B), interference of DPAH with other common ions and pesticides (C), and a comparison of the interfering signal with the standard DPAH signal (D).

measurement of DPAH. Hence, we omitted those peaks for the calibration data. Fig. 7B shows the calibration curve for the determination of DPAH<sup>+</sup>, which is directly proportional to the concentration of DPAH. From the calibration plot, the lowest detection limit and the linear concentration range were calculated as 30 nM and 0.1–35 μM. This result is highly comparable with previously reported DPAH sensors, which showed a detection limit around 3.9 μM [22]. In contrast, the developed SrMoO<sub>4</sub>/GCE sensor exhibited a very low detection limit and an acceptable sensitivity of 2.165 μA μM<sup>-1</sup> cm<sup>-2</sup>. Hence, the reported SrMoO<sub>4</sub>/GCE sensor allows low-level electrochemical detection of DPAH. However, the selectivity is the major problem with detecting the DPAH<sup>+</sup> in this study. Therefore, the selectivity of the developed sensor electrode was studied in common ions and some pesticides. Those pesticides are commonly used in agriculture; further, the common ions usually exist in tap water. Fig. 7C shows the DPV curves of DPAH<sup>+</sup> detection in the presence of a 10-fold excess of chlorpyrifos, carbofuran, diuron, and urea and a 100-fold excess of Na<sup>+</sup> and Cl<sup>-</sup>. The tested substances interfere strongly with the electrochemical activity of DPAH<sup>+</sup>, which influences 103–107% of the interference signal. The interference signal is plotted for the interfering compounds where the DPAH signal is fixed as 100% for com-

parison (Fig. 7D). These relative 3–7% signals imply that the aforementioned substances are interfere strongly with DPAH<sup>+</sup>. Particularly, the urea causes maximum interference with the signal of 107%. This high contribution was ascribed from the involvement of urea with the oxidation of secondary products (DPB). Predominantly, the lone pair of nitrogen (from urea) interacts with the radical cation (DPAH<sup>+</sup>) and increases the peak current of oxidation peak 6. This will further interact with radical generation; thus, the peak of DPAH<sup>+</sup> deviated from its original response. The same thing happened for other interferents such as Na<sup>+</sup> and Cl<sup>-</sup>, here, also, the cation and anion interfered in similar ways. The acceptable interference current change was less than 3% for the commercial sensor devices; however, the present work shows more than 3%. However, less than a 7% signal was allowed for the initial laboratory testing [34,41,42]. Further, this compound needs to modify its structure or surface characteristics to get effective selectivity.

#### 4. Conclusions

In summary, we have demonstrated the photocatalytic and electrocatalytic properties of SrMoO<sub>4</sub> for the degradation and

determination of DPAH. The UV–vis studies showed that the photodegradation of DPAH reached 99% in 45 min. The controlled experiments showed that the optimal catalyst loading, concentration, and pH are 50 mg/mL, 20 mg/L, and 12, respectively, for the effective degradation. The rate of degradation mainly depends on the primary active species OH<sup>•</sup> radicals, which is confirmed by the scavenger profile analysis. Moreover, the electrochemical determination of DPAH was demonstrated by DPAH<sup>•+</sup> and indicated a linear range of 0.1–35 μM a lowest detection limit of 30 nM. However, the developed sensing tool lacks selectivity: as discussed above, DPAH<sup>•+</sup> is highly reactive toward both anions and cations. The tested substances interfere strongly with the electrochemical activity of DPAH<sup>•+</sup>, which influences 103–107% of the interference signal. This 7% interfering signal restricts this device for real-time analysis; however, it is acceptable for the laboratory. Therefore, the selectivity of the developed sensor should be improved by introducing some other metals or altering its surface phenomena. In the future, it is necessary to focus on the design of this compound and its application to DPAH determination.

### Acknowledgment

This project was supported by the Ministry of Science and Technology of Taiwan, Republic of China.

### References

- [1] A.W. Sleight, *Acta Crystallogr. Sect. B* 28 (1972) 2899–2902.
- [2] N. Sharma, K.M. Shaju, G.V. Subba Rao, B.V.R. Chowdari, Z.L. Dong, T.J. White, *Chem. Mater.* 16 (2004) 504–512.
- [3] S. Neeraj, N. Kijima, A.K. Cheetham, *Chem. Phys. Lett.* 387 (2004) 2–6.
- [4] E. Cavalli, P. Boutinaud, R. Mahiou, M. Bettinelli, P. Dorenbos, *Inorg. Chem.* 49 (2010) 4916–4921.
- [5] V.S. Marques, L.S. Cavalcante, J.C. Sczancoski, A.F.P. Alcantara, M.O. Orlandi, E. Moraes, E. Longo, J.A. Varela, M.S. Li, M.R.M.C. Santos, *Cryst. Growth Des.* 10 (2010) 4752–4768.
- [6] B.P. Singh, A.K. Parchur, R.S. Ningthoujam, A.A. Ansari, P. Singh, S.B. Rai, *Dalton Trans.* 43 (12) (2014) 4770–4778.
- [7] D. Errandonea, R.S. Kumar, M. Xinghua, C. Tu, *J. Solid State Chem.* 181 (2) (2008) 355–364.
- [8] E. Gürmen, D. Eugene, J.S. King, *J. Chem. Phys.* 55 (3) (1971) 1093–1097.
- [9] A. Cameirão, D. René, E. Fabienne, G. Frédéric, *J. Cryst. Growth* 310 (18) (2008) 4152–4162.
- [10] T. Thongtem, S. Kungwankunakorn, B. Kuntalue, A. Phuruangrat, S. Thongtem, *J. Alloys Compd.* 506 (2010) 475–481.
- [11] T. Thongtem, A. Phuruangrat, *J. Nanopart. Res.* 12 (2010) 2287–2294.
- [12] G. Zhang, S. Yu, Y. Yang, W. Jiang, S. Zhang, B. Huang, *J. Cryst. Growth* 312 (2010) 1866–1874.
- [13] J.C. Sczancoski, L.S. Cavalcante, M.R. Joya, J.A. Varela, P.S. Pizani, E. Longo, *Chem. Eng. J.* 140 (2008) 632–637.
- [14] V. Thangadurai, C. Knittlmayer, W. Weppner, *Mater. Sci. Eng., B* 106 (2004) 228–233.
- [15] B.D. Whitaker, *Postharvest Biol. Technol.* 18 (2000) 91–97.
- [16] E.F.S. Authority, Conclusion on the peer review of the pesticide risk assessment of the active substance Pepino mosaic virus strain CH2 isolate 1906, *EFSA J.* 13 (1) (2015).
- [17] European Food Safety Authority, *EFSA J.* 9 (2011) 2336.
- [18] J. Dallüge, V.R. Martijn, B. Jan, R.J.J. Vreuls, A. Udo, *J. Chromatogr. A* 965 (1) (2002) 207–217.
- [19] B. Saad, H.H. Noor, I.S. Muhammad, H.H. Noor, A. Ahamad, A. Norhayati, *Food Chem.* 84 (2) (2004) 313–317.
- [20] Y. Tong, W. Zhuping, Y. Chengdui, Y. Jianyuan, Z. Xinrong, Y. Shijie, D. Xinyuan, X. Yucai, W. Yuxiu, *Analyst* 126 (4) (2001) 480–484.
- [21] B. Hemmateenejad, A. Morteza, S. Fayeze, *Spectrochim. Acta Mol. Biomol. Spectrosc. A* 67 (3) (2007) 958–965.
- [22] V.L.V. Granado, G.C. Manuel, F.S. César, M. Teresa, S.R. Gomes, R. Alisa, J. Cecilia, *J. Anal. Chim. Acta* 809 (2014) 141–147.
- [23] M. Shamsipur, H. Bahram, J.J. Naser, M.M. Kamran, *J. Photochem. Photobiol.: Chem.* 299 (2015) 210–217.
- [24] J. Vinoth Kumar, R. Karthik, S.M. Chen, V. Muthuraj, C. Karuppiah, *Sci. Rep.* 6 (2016) 1–8.
- [25] R. Karthik, J. Vinoth Kumar, S.M. Chen, C. Karuppiah, Y.H. Cheng, V. Muthuraj, *ACS Appl. Mater. Interfaces* 9 (2017) 6547–6559.
- [26] D. Chen, K. Tang, F. Li, H. Zheng, *Cryst. Growth Des.* 6 (2006) 247–252.
- [27] T.T. Basiev, A.A. Sobol, P.G. Zverev, L.I. Ivleva, V.V. Osiko, R.C. Powell, *Opt. Mater.* 11 (1991) 307–314.
- [28] T.T. Basiev, A.A. Sobol, Y.K. Voronko, P.G. Zverev, *Opt. Mater.* 15 (2000) 205–216.
- [29] S.I. Woo, J.S. Kim, H.K. Jun, *J. Phys. Chem. B* 108 (2004) 8941–8946.
- [30] G. Tyuliev, S. Angelov, *Appl. Surf. Sci.* 32 (1988) 381–391.
- [31] S. Hufner, *Photoelectron Spectroscopy, Principles and Applications*, Springer, Berlin, 2003.
- [32] M. Naeem, S.K. Hasanain, M. Kobayashi, Y. Ishida, A. Fujimori, B. Scott, S. Ismat Shah, *Nanotechnology* 17 (2006) 2675.
- [33] S.J. Liang, S.Y. Zhu, Y. Chen, W.M. Wu, X.C. Wang, L. Wu, *J. Mater. Chem.* 22 (2012) 2670–2678.
- [34] N. Karikalan, R. Karthik, S.M. Chen, A.C. His, *Sci. Rep.* 7 (2017) 45924, <http://dx.doi.org/10.1038/srep45924>.
- [35] M. Velmurugan, N. Karikalan, S.M. Chen, Y.H. Cheng, C. Karuppiah, *J. Colloid Interface Sci.* 500 (2017) 54–62.
- [36] G. Inzelt, *J. Solid State Electrochem.* 6 (2002) 265–271.
- [37] H. Yang, J.B. Allen, *J. Electroanal. Chem. Interfacial Electrochem.* 306 (1–2) (1991) 87–109.
- [38] N. Vettorazzi, J.J. Silber, L. Sereno, *J. Electroanal. Chem.* 125 (1981) 459–475.
- [39] D. Serve, *Electrochim. Acta* 21 (1976) 1171–1181.
- [40] J. Guay, L.H. Dao, *J. Electroanal. Chem.* 274 (1989) 135–142.
- [41] M. Velmurugan, N. Karikalan, S.M. Chen, Z.C. Dai, *J. Colloid Interface Sci.* 490 (2017) 365–371.
- [42] N. Karikalan, M. Velmurugan, S.M. Chen, C. Karuppiah, K.M. Al-Anazi, M.A. Ali, B.S. Lou, *RSC Adv.* 6 (2016) 71507–71516.